

Aerodynamic Modeling for Thrust Vector Control Rocketry

Rushil Negandhi*, Jackson Meyers†, Sameer Sheth‡, Hector Sanchez§
Georgia Institute of Technology, Atlanta, Georgia, 30332

Guidance, navigation, and control (GNC) systems are widely used in the aerospace industry for vehicle stabilization and control. In rockets, methods such as thrust vector control (TVC) allow for controlled maneuvers and active stabilization. However, rocket fins also passively stabilize the trajectory by inducing restoring moments in the roll, pitch, and yaw axes. These forces and moments can interfere with the GNC system. Aspects of both static and dynamic stability must be considered by characterizing the vehicle's natural aerodynamic response to disturbances such as angle of attack (AOA) and rotation rates. The GNC team under the Georgia Institute of Technology Ramblin' Rocket Club (RRC) aims to implement a jet vane TVC system on a solid-propellant rocket. Computational fluid dynamics (CFD) methods were used to develop a nonlinear regression that predicts aerodynamic forces and moments associated with static stability. Unstructured mesh generation and simulations were performed using the commercial CFD software Ansys Fluent with a pressure-based solver and the $k - \omega$ SST turbulence model. The rocket was simulated under varying angles of attack from 0 to 5 degrees and Mach numbers from 0.2 to 0.7. To characterize dynamic stability responses to roll, pitch, and yaw rates, a combination of theoretical and empirical relations was used. The resulting combined aerodynamic model was used to model the rocket's trajectory and tune jet vane control parameters. The insights from this process provide a methodology for feasible, medium-fidelity analysis of the static and dynamic stability of rockets.

I. Nomenclature

$[A, B, C, D]$	=	Regression model coefficients
a	=	Lift curve slope, 1/rad
C_D	=	Drag coefficient
C_L	=	Lift coefficient contribution due to angle of attack
$(C_L)_q$	=	Lift coefficient contribution due to pitch rate
C_M	=	Pitching moment coefficient contribution due to angle of attack
$(C_M)_q$	=	Pitching moment coefficient contribution due to pitch rate
$(C_l)_p$	=	Rolling moment coefficient contribution due to roll rate
c_r	=	Fin root chord length, ft
c_t	=	Fin tip chord length, ft
\bar{c}	=	Mean aerodynamic chord length, ft
d	=	Reference body diameter, ft
k	=	Turbulent kinetic energy, ft^2/s^2
$[l, M, N]$	=	Moments in roll, pitch, yaw axes, lb-ft
M_∞	=	Freestream Mach number
N	=	Number of fins
$[p, q, r]$	=	Rotation rates in roll, pitch, yaw axes, rad/s
r_t	=	Radius at fin tip, ft
s	=	Span of one fin, ft
S_{ref}	=	Reference area, combined area of two fins, ft^2
w	=	Tangential velocity observed by fin aerodynamic center due to pitch rate, ft/s

*Undergraduate Member, GT Ramblin' Rocket Club, Daniel Guggenheim School of Aerospace Engineering, AIAA Student Member, 1406070

†Undergraduate Member, GT Ramblin' Rocket Club, Daniel Guggenheim School of Aerospace Engineering, AIAA Student Member, 1809877

‡Undergraduate Member, GT Ramblin' Rocket Club, Daniel Guggenheim School of Aerospace Engineering, AIAA Student Member, 1603262

§Undergraduate Member, GT Ramblin' Rocket Club, Daniel Guggenheim School of Aerospace Engineering, AIAA Student Member, 1419750

V_∞	=	Freestream velocity, ft/s
x_{AC}	=	Center of gravity to fin aerodynamic center distance, ft
x_{CG}	=	Nosetip to center of gravity distance, ft
x_f	=	Center of gravity to fin leading edge distance, ft
x_l	=	Nosetip to fin trailing edge distance, ft
\bar{y}	=	Spanwise location of mean aerodynamic chord from fin root chord, ft
y^+	=	Non-dimensionalized distance from wall for turbulence modeling
α	=	Angle of attack, deg
α_q	=	Effective angle of attack observed by fin due to pitch rate, deg
ϵ	=	Turbulence dissipation rate, ft^2/s^3
Γ_c	=	Fin mid-chord sweep angle, deg
λ	=	Taper ratio, c_t/c_r
ω	=	Specific turbulence dissipation rate, 1/s
ν_T	=	Kinematic eddy viscosity, ft^2/s
ν	=	Kinematic molecular viscosity, ft^2/s

II. Introduction

In the field of guidance, navigation, and control (GNC) systems in small-scale rocketry, various active control and stabilization techniques can be implemented. These include aerodynamic control surfaces, momentum control devices, and thrust vector control (TVC). Unlike the former examples, TVC does not require the use of extensive aerodynamic analysis and experimentation, such as wind tunnel testing, which can be infeasible for student rocketry projects or other low-cost endeavors. However, aerodynamic modeling of the vehicle's passive stability system is still vital in order to address interferences with the active control system.

Both static and dynamic stability analysis must be considered when modeling a vehicle's response to disturbances. Static stability consists of the instantaneous aerodynamic response to changes in angle of attack (AOA). This can be readily modeled using computational fluid dynamics (CFD). Dynamic stability, on the other hand, involves the natural oscillations of the vehicle as a result of the AOA and rotation rates. This is a much greater challenge to model via CFD due to the motion of the vehicle [1].

In rockets, the passive stability system is largely controlled by the rocket fins [2]. Figure 1 shows the mechanism by which a rocket can provide a lifting force when disturbed at an AOA, consequently generating a restorative moment. This is analogous to a wing producing a lift force that induces a negative pitching moment when the center of pressure is downstream of the center of gravity.

The GNC team of Georgia Tech's Ramblin' Rocket Club (RRC) aims to implement a TVC system to build an actively stabilized rocket designed to fly over Mach 0.6 to approximately 10,000 ft. This requires complete modeling of the vehicle's aerodynamics since all trajectory and controls simulations are internally developed and depend on knowledge of aerodynamic loads in flight. While existing software such as OpenRocket or RASAero contain low-fidelity methods to predict aerodynamics, they have limited controller implementation capability and insufficient aerodynamic modeling for GNC [2, 3]. The full aerodynamic model has the capability to output lift, drag, and moments with the following inputs: AOA, rotation rates, velocity, and altitude. This paper outlines the prediction of aerodynamic forces and moments related to static stability at any flight condition using CFD and nonlinear regression. Damping coefficients related to dynamic stability are also approximated using theoretical and semi-empirical methods.

Since the rocket is symmetric across two longitudinal planes, forces and moments along the pitch and yaw axes are identical. For simplicity, this aerodynamic model gives a single set of force and moment values along the pitch axis. The flight is assumed to be planar and two-dimensional, implying rotation solely about the pitch axis. The axes and sign conventions used in this paper are defined in Fig. 2.

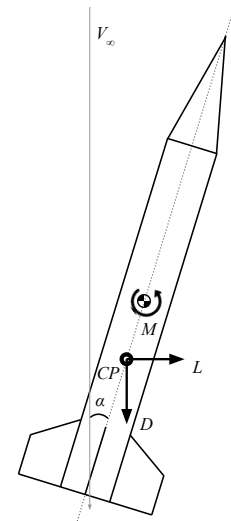


Fig. 1 Net aerodynamic forces (L , D) acting at the center of pressure (CP) generate a restorative pitching moment M about the center of gravity (CG).

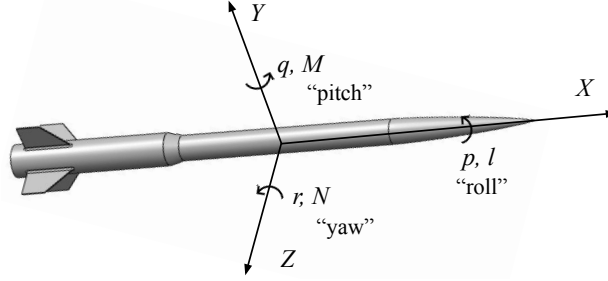


Fig. 2 Axes and sign conventions of rotation rates and moments; the models assume flight in only the XZ plane for simplicity.

Equations (1a)-(1d) show the components of lift force, drag, and restoring pitching moment coefficients due to AOA or rotation rates considered.

$$C_{L,\text{total}} = C_L + (C_L)_q \quad (1a)$$

$$C_{D,\text{total}} = C_D \quad (1b)$$

$$C_{M,\text{total}} = C_M + (C_M)_q \quad (1c)$$

$$C_{l,\text{total}} = (C_l)_p \quad (1d)$$

Note that forces and moments due to rate of angle of attack, Magnus effect, and other nonlinear phenomena were neglected for simplicity. Additionally, drag due to pitch rate is assumed to be negligible. A dependency on Mach number is also integrated into the above coefficients. Most of the coefficient components are nonlinear functions of variables such as α , M_∞ , and x_{CG} . The coefficients C_L , C_D , and C_M are discussed in the Section III, while $(C_L)_q$, $(C_M)_q$, and $(C_l)_p$ are discussed in Section IV.

III. Static Stability

To determine lift, drag, and pitching moment due to AOA and Mach number, the rocket is simulated using CFD under conditions of 0, 2.5, and 5 degrees AOA and Mach numbers of 0.2 to 0.7 by intervals of 0.1 for a total of 18 simulations. The relatively low range and resolution of AOA conditions is acceptable due to the highly linear nature of aerodynamic forces at a small AOA, which is expected in a nominal rocket trajectory. However, a more complete range of Mach numbers is required to accurately capture nonlinear compressibility effects.

A. Geometry Development

To begin the simulation process, the rocket model was defeatured in SolidWorks; this is an essential process in CFD analysis to alleviate added computational expense attributed to small, often unnecessary, features. Components such as fasteners, holes, and launch lugs were removed to simplify the meshing process. The simplified model is the same one shown in Fig. 2.

The resulting geometry was then imported into Ansys SpaceClaim to build the fluid domain and perform other geometry corrections. Shown in Fig. 3, a spherical farfield with a radius approximately 15 times the rocket length was chosen to minimize boundary interference, maintain compactness, and simplify the mesh. A subsequent convergence study showed that a C-shaped domain lengthened in the downstream direction had no significant impact on results. The nosecone face was split 3 inches from the nosetip, enabling a separate, more refined surface mesh at the nosetip which is beneficial to improve inflation

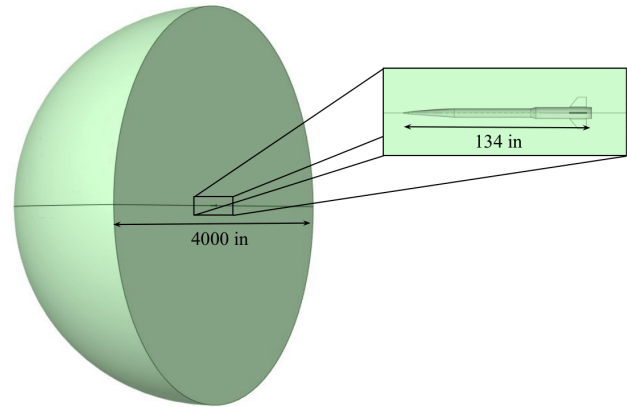


Fig. 3 Simulated fluid domain is sufficiently large to accurately model the farfield boundary condition.

layer meshing quality by preventing stair-stepping. Assuming no angular velocities, the model has one plane of symmetry, so the model was cut at the XZ plane to improve computational efficiency by reducing the size of the domain by half. The results produced from this geometry were later multiplied by two to account for this change in the domain.

B. Methods

CFD simulations were performed in Ansys Fluent. The flow of interest is in the subsonic compressible regime. Continuum flow can be assumed because the rocket remains at low altitudes, and steady-state simulations were run as transient effects were assumed to be negligible. Hence, the governing equations of this simulation are the steady, compressible forms of the Navier-Stokes equations. A pressure based solver was used for faster convergence and performance for a wide range of Mach numbers [4]. To account for the strong coupling between the pressure and velocity terms, the coupled scheme was employed. Spatial discretization was performed using a second-order upwind scheme which performs better with unstructured, polyhedral meshes [5]. Finally, gradient computation was performed using the least-squares cell-based method as it performs better with the relatively skewed cells of the unstructured mesh. Moreover, the least-squares method provides the same level of accuracy as the Green-Gauss node-based method but is more computationally efficient [5].

C. Turbulence Modeling

Turbulence is a significant consideration in high Reynolds number flows such as this one. Turbulence modeling is necessary to simplify the computational cost of the CFD model, as a direct numerical simulation (DNS) approach is impractical and unnecessary for this simulation. Instead, the Reynolds-averaged Navier-Stokes (RANS) equations time-average the Navier-Stokes equations by simplifying velocity components into a sum of mean velocities and turbulent fluctuations, resulting in Reynolds stress terms that represent fluctuating velocity components. Expressing these terms as a function of eddy viscosity by invoking the Boussinesq Hypothesis, the closure problem is reduced to using a turbulence model that determines a value for ν_T . This class of turbulence models is known as eddy viscosity models [6].

A commonly used eddy viscosity turbulence model is the $k - \omega$ SST model, which calculates ν_T using a ratio of turbulent kinetic energy to specific turbulence dissipation rate. The $k - \omega$ SST model uses a blending function in the transport equation for ω , using the $k - \epsilon$ model away from the wall and the $k - \omega$ model near the wall, combining the strengths of both models. Furthermore, a viscosity limiter blending function is used in near-wall flows, which prevents overestimation of the wall shear stress, a drawback of the $k - \omega$ model [7]. In a variety of flows, these characteristics allow the $k - \omega$ SST model to outperform both the $k - \epsilon$ model, which suffers from unreliable damping for near-wall modeling, and the $k - \omega$ model, which is too sensitive to freestream turbulence conditions and overpredicts ω close to the wall [8]. This formulation makes the $k - \omega$ SST model fit for external aerodynamics featuring adverse pressure gradients, separated flows, and a need for accurate skin friction drag estimation [9]. Another option considered was the Spalart-Allmaras turbulence model. As a one equation model that estimates ν_T directly, the Spalart-Allmaras formulation calculates a linear approximation, $\tilde{\nu}_T$, using a transport equation and a correcting function to model the viscous damping effects near the wall [10, 11]. While this makes the model more computationally efficient, it lacks the accuracy of the $k - \omega$ SST model, especially in complex separated flows. Both models were tested, but the $k - \omega$ SST model was ultimately chosen due to considerable difference in results and acceptable computational expense.

To achieve accurate near-wall modeling, the $k - \omega$ SST model requires y^+ to be approximately 1. This is a requirement to directly resolve the viscous sublayer, which ranges from $0 < y^+ < 5$. The height of the first layer along the wall in the mesh must not significantly exceed $y^+ = 1$ because this will cause the turbulence model to resort to less accurate wall functions for near-wall modeling [5]. Enforcing this requirement is further described in Section III.D.

D. Meshing

An unstructured mesh was created using Ansys Fluent. Meshing parameters were based on mesh convergence studies and limitations of computational resources. Inflation layers were created using the last-ratio method, enabling direct specification of the first-layer height. The number of layers and first layer height were iterated upon until a y^+ on the order of 1 was achieved and the boundary layer was contained within the inflation layer mesh, as shown in Fig. 4. A finer mesh was implemented at the fins, which are the primary lifting surfaces of the vehicle and therefore require more refinement. Mesh quality was ensured by verifying that skewness did not exceed 0.7 and orthogonal quality was at least 0.10. A summary of the mesh parameters, quality, and cell count is shown in Table 1.

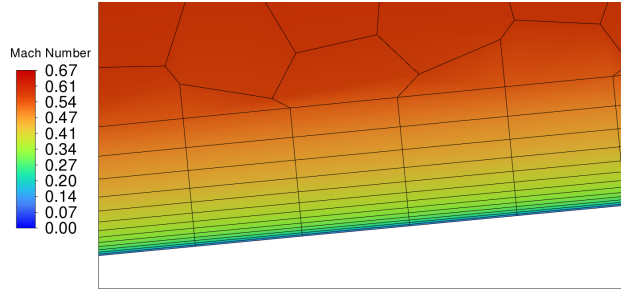


Fig. 4 Boundary layer is contained within the inflation layer mesh cells.

Table 1 Mesh Sizing Parameters

Components	Surface Local Sizing (in)
Nosetip	0.1
Nosecone	0.5
Body	1
Aft Face	0.25
Fins	0.075
Inflation Layers	13 layers, 0.0008 in first layer height
Cell count	3.84 million
Maximum Skewness	0.50
Minimum Orthogonal Quality	0.15

E. Boundary Conditions

In compressible flows, the pressure farfield boundary conditions is generally preferable, provided that the boundaries of the domain are sufficiently far as they are intended to represent the conditions an infinite distance away from the body [5]. Instead of changing the AOA by tilting the rocket model, the flow direction was altered when establishing the boundary condition to define AOA. This eliminates the need to edit the geometry and create separate meshes for each condition. The freestream Mach number, static pressure, and temperature were also input in the farfield boundary conditions. Sea level conditions were assumed where necessary as the resulting coefficients are normalized to density, incorporating any altitude effects. The turbulence viscosity ratio (ν_T/ν) and the turbulence intensity, which is a ratio of turbulence velocity fluctuations to mean velocity, are set at 1 and 1%, respectively. These are typical values for external aerodynamics simulations [12]. The second boundary condition is the rocket itself, which is modeled as a no-slip wall. To account for surface roughness, a sand height of $60 \mu\text{m}$ was used to approximate a regular paint finish [2].

F. Results and Discussion

After running simulations to gather aerodynamic force and moment coefficients at each condition, regression models were fit to the data to achieve analytical expressions. The regression model must account for the two independent variables: AOA and Mach number. The first step in solving the regression problem is to clean the data. Since the CFD simulations directly provided the lift, drag and pitching moment data, these were converted to non-dimensionalized coefficients by dividing by dynamic pressure and S_{ref} for force coefficients, and additionally dividing by d for moment coefficients. The next step is to determine which features should be included in the model for lift, drag, and pitching moment coefficients.

The lift coefficient is known to change linearly with AOA for thin airfoils at low angles of attack. However, compressibility effects are more complex. The Prandtl-Glauert compressibility correction is often used to approximate this relation, given by Eq. (2) [13].

$$C_L = \frac{a\alpha}{\sqrt{1 - M_\infty^2}} \quad (2)$$

Observing that the model had poor fit, an additional constant B was added to the denominator. This is reflective of other compressibility corrections such as the Karman-Tsien Rule and Laitone's Rule, which include a secondary function of M added to the denominator [14, 15]. For the data found in the simulations, approximating this secondary function to a constant was sufficient to achieve low error. Additionally, the numerator was replaced by a general constant A to account for these corrections.

$$C_L(\alpha, M_\infty) = \left(\frac{A}{B + \sqrt{1 - M_\infty^2}} \right) \alpha \quad (3)$$

For purely subsonic flows, drag generally has a quadratic relation with lift [13]. However, for the data found, C_D was found to be highly linear with C_L , which is proportional to α . Because C_D is only slightly sensitive to compressibility effects before the transonic regime, it was assumed to be constant with Mach number for the regression model. Hence, we have

$$C_D(\alpha) = A\alpha + B \quad (4)$$

By definition, the pitching moment is the combination of lift and drag forces multiplied by a moment arm. There is also a small correction of force directions with AOA, but this can be neglected. Hence, the expression for $C_M(\alpha, M)$ is the sum of $C_L(\alpha, M)$ and $C_D(\alpha)$ multiplied by a constant representing the moment arm, which is grouped into the already existing constants.

$$C_M(\alpha, M_\infty) = \left(\frac{A}{B + \sqrt{1 - M_\infty^2}} \right) \alpha + C\alpha^2 + D \quad (5)$$

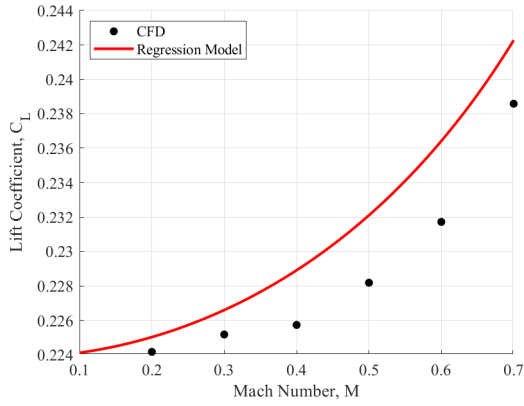
However, Eq. (5) does not satisfy the condition $C_M(\alpha, M_\infty) = 0$. In other words, the model predicts a nonzero pitching moment even though the rocket is not at an AOA, which is non-physical. To correct this, the α term is factored out without treating the constant D , as shown in Eq. (6). This model represents the moment about the initial center of gravity with a full motor, but in-flight changes in center of gravity can be accounted for by performing a moment transfer.

$$C_M(\alpha, M_\infty) = \alpha \left(\frac{A}{B + \sqrt{1 - M_\infty^2}} + C\alpha + D \right) \quad (6)$$

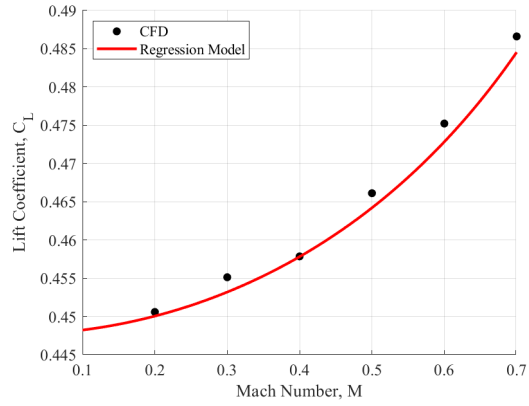
Regression models using Eqs. (3), (4), and (6) were applied to the data gathered from running the CFD simulations. This was performed in MATLAB using least-squares nonlinear curve fitting to minimize error. The final coefficients used in the model and the corresponding mean relative error (MRE) are shown in Table 2. Figs. 5-8 show the results of the regression model and comparisons to simulated data.

Table 2 Regression model coefficients and MRE.

Coefficient	C_L	C_D	C_M
A	0.33592	0.01383	0.21441
B	2.7509	0.14023	0.57737
C	-	-	0.00030
D	-	-	-0.03344
MRE (%)	0.801	1.384	0.758

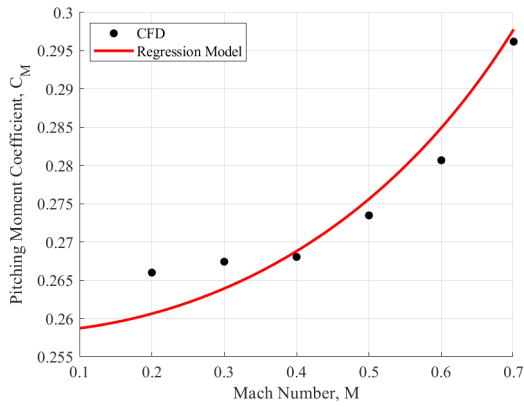


(a) $\alpha = 2.5^\circ$

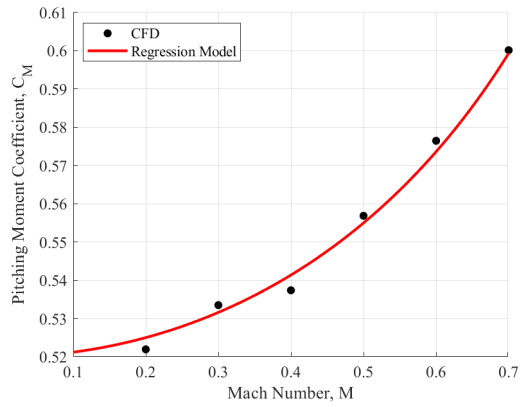


(b) $\alpha = 5^\circ$

Fig. 5 Lift coefficient comparison of regression model with CFD data with respect to Mach number for two angles of attack.



(a) $\alpha = 2.5^\circ$



(b) $\alpha = 5^\circ$

Fig. 6 Pitching moment coefficient comparison of regression model with CFD data with respect to Mach number for two angles of attack.

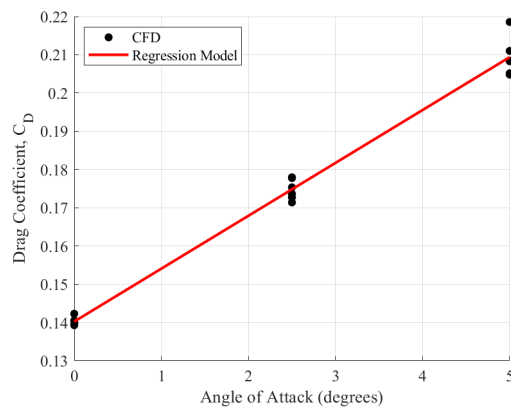


Fig. 7 Drag coefficient comparison of regression model with CFD data with respect to angle of attack.

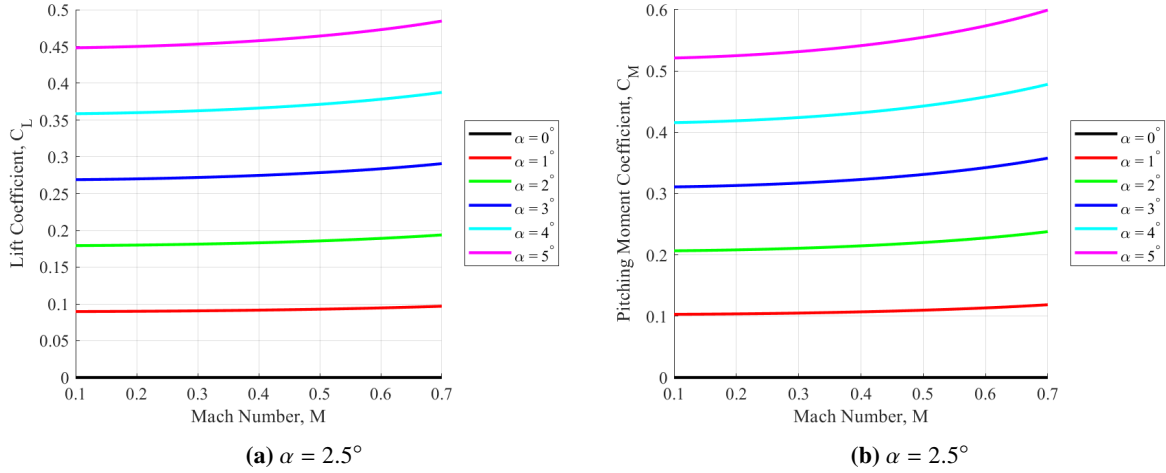


Fig. 8 Regression model results for lift and pitching moment coefficients as a function of Mach number and angle of attack.

As shown in Table 2, the error between the simulation results and the predicted values from the regression model is minimal, on the order of 1%. This verifies that the functions used for the regression model can sufficiently predict aerodynamic force and moment coefficients in the tested conditions. Although controls are implemented before the velocity reaches Mach 0.2, the modified Prandtl-Glauert rule that was incorporated enables a more accurate extrapolation at low Mach numbers.

The main source of error for lift coefficient prediction is not the AOA relation, which is highly linear, but instead the Mach number dependency. This can be attributed to the fact that compressibility correction relations are approximations that do not necessarily reflect viscous effects or complex geometry.

For drag, the result of a linear relation as opposed to a quadratic relation with AOA is significant. The quadratic relationship between C_D and C_L is due to induced drag, where $C_{Di} \propto C_L^2 \propto \alpha^2$. Induced drag is caused by wing tip vortices and downwash when a lifting surface is producing nonzero lift. For this rocket, there are two potential reasons that may explain why drag does not exhibit a linear relationship with AOA. First, the fins have a low aspect ratio of approximately 4. Lanchester-Prandtl lifting-line theory, which governs the induced drag relation described, fails as it is only valid for high aspect ratio wings [13]. Second, parasitic drag from the entire rocket body has a much larger contribution than induced drag, which is produced only by the fins. The relationship between drag and AOA could deviate from this quadratic relationship for this reason. Drag polars sometimes use a 3-parameter model which includes a term proportional to C_L that could account for this; however, in this case, a purely linear model was sufficient.

A more concerning issue is the potential error of CFD results compared to aerodynamic forces and moments experienced in flight. A major contributor to this could be the defeaturing of the rocket model. Components such as launch lugs and the jet vanes assembly located at the aft end of the rocket were approximated or not modeled at all due to geometric intricacy that would complicate the meshing process. In flight, these would generate additional drag. While some discrepancies here are unavoidable, the rocket will be thoroughly sanded and painted to ensure that the roughness height generally matches the CFD rocket model. In terms of stability, drag has a much smaller contribution to the restoring moment than lift as it remains mostly in the axial direction. Therefore, some error in drag will not greatly affect stability and the control system interaction. Finally, the avionics and controls team, responsible for modeling the trajectory of the rocket, has shown that the rocket performs well despite considerable uncertainties after running numerous Monte Carlo simulations.

Figure 9 shows Mach flow contours produced by the simulation. At a 5 degree AOA and Mach 0.6, the flow accelerates considerably but supersonic flow is not reached, preventing any nonlinear transonic effects. Figure 9b shows flow separation due to the rectangular geometry of the airfoil in addition to a considerably large wake. This can be alleviated by using a rounded leading edge airfoil; however, this creates manufacturing challenges and the relatively low thickness-chord ratio prevents excessive aerodynamic efficiency loss due to a rectangular airfoil.

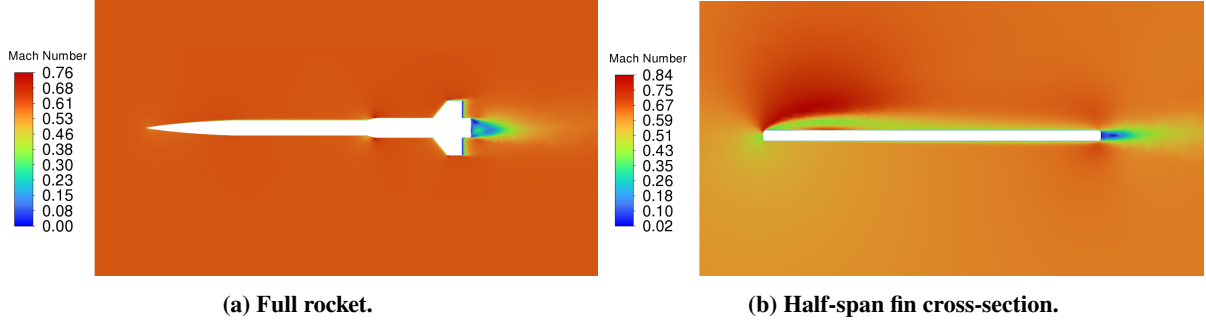


Fig. 9 Mach number contours at $\alpha = 5^\circ$ and Mach 0.6.

IV. Dynamic Stability

A. Longitudinal Stability

When an angular pitch velocity is induced on a rocket, each part of the rocket experiences a lateral velocity that starts from zero at the center of gravity and increases in magnitude moving towards the ends of the rocket. The combination of a freestream velocity component and a lateral velocity component induces an effective angle of attack, and consequently, a lift force that primarily acts on the fins. There is a change in drag and potential body lift due to this phenomenon, but these are small compared to other components and were assumed to be negligible. Fig. 10 shows a visualization of lift and restoring moment due to pitch rate.

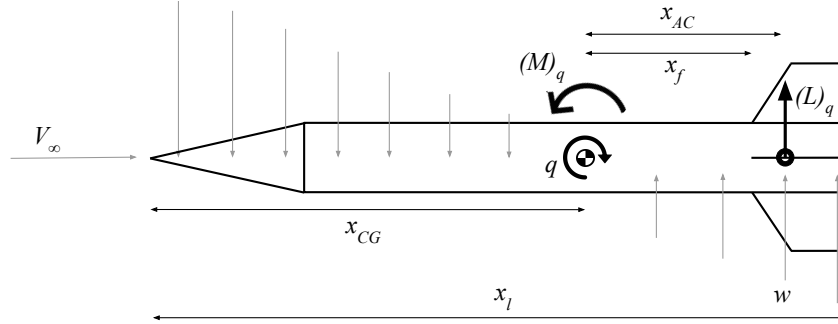


Fig. 10 Angular pitch rate induces a normal component to the freestream velocity, causing the fins to produce a force and restoring moment in a direction opposite to the pitch rate.

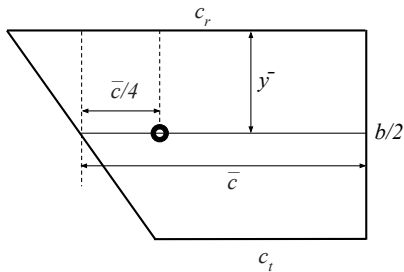


Fig. 11 Position of aerodynamic center and MAC on a single fin.

$(L)_q$ is assumed to act at the aerodynamic center of the fins, which occurs at the quarter-chord location along the mean aerodynamic chord (MAC). The location of the MAC along the spanwise axis and the length of the MAC for wings assuming the loading is proportional to the wing chord is given by Eq. (7) and shown in Fig. 11 [16].

$$\bar{y} = s + \frac{1 + 2\lambda}{3(1 + \lambda)} \quad (7)$$

$$\bar{c} = \frac{2c_r}{3} \frac{1 + \lambda + \lambda^2}{1 + \lambda} \quad (8)$$

From Figs. 10 and 11, the distance from the center of gravity to the aerodynamic center of the fins, which is also the moment arm and radius of angular velocity, is given by Eq. (9).

$$x_{AC} = x_l - x_{CG} - c_r + \frac{\bar{y}}{c_r - c_t} + \frac{\bar{c}}{4} \quad (9)$$

Assuming that the rocket is not already at some angle of attack, the effective angle of attack caused by this pitching rate is then given by Eq. (10), where the numerator represents the instantaneous lateral velocity acting at the aerodynamic center caused by the pitch rate.

$$\alpha_q = \tan^{-1} \left(\frac{w}{V_\infty} \right) = \tan^{-1} \left(\frac{q(x_l - x_{CG} - c_r + \frac{\bar{y}}{c_r - c_t} + \frac{\bar{c}}{4})}{V_\infty} \right) \quad (10)$$

The lift curve slope for low aspect ratio fins is given by the semi-empirical relation shown in Eq. (11) [17].

$$C_{L\alpha_q} = \frac{2\pi \left(\frac{s^2}{S_{\text{ref}}} \right)}{1 + \sqrt{1 + \left(\frac{s^2 \sqrt{1 - M_\infty^2}}{(S_{\text{ref}}/2) \cos(\Gamma_c)} \right)^2}} \quad (11)$$

Then, the lift coefficient due to pitch rate can be written as shown in Eq. (12), where $C_{L\alpha_q}$ and α_q are given by Eqs. (11) and (10), respectively.

$$(C_L)_q = C_{L\alpha_q} \alpha_q \quad (12)$$

Finding the moment coefficient is found by multiplying the force coefficient by a non-dimensionalized moment arm. Equation (13) shows the moment coefficient contribution due to pitch rate.

$$(C_M)_q = \frac{x_{AC}}{d} (C_L)_q \quad (13)$$

B. Roll Stability

The passive roll stability mechanism is similar to that which is described in Section IV.A. As the rocket rolls, the fins see a component of velocity normal to the freestream velocity equal to the angular roll velocity of the rocket multiplied by the radius of the velocity. The simulation software OpenRocket uses a formulation for the damping moment coefficient based on discretizing the fin area into strips, which is a sufficient approximation for this model [2]. This formulation is shown in Eq. 14. It is important to address that no net forces are produced, as lift produced by opposite-sided fins cancel out.

$$(C_l)_p = \frac{2\pi p N}{(S_{\text{ref}}/2) d V_\infty \sqrt{1 - M_\infty^2}} \left(\frac{c_r + c_t}{2} r_t^2 + \frac{c_r + 2c_t}{3} r_t s^2 + \frac{c_r + 3c_t}{2} s^3 \right) \quad (14)$$

C. Discussion

Damping parameters are difficult to characterize in many systems; in this scenario, modeling a rotating fluid or mesh in CFD proved to be too challenging for the scope of this project due to excessive computational expense from a full rocket mesh and the potential need for transient simulations. While the methods presented in this paper are reasonable estimations, they make numerous assumptions and may not capture all flow effects. For example, body lift and drag were neglected for the pitch dynamic stability formulation. Despite this, forces and moments due to pitch and roll rates were found to be small under nominal flight conditions when simulated. In fact, dynamic pitch stability is usually not significant until apogee, long after controlled flight [2]. Roll restoring moments are important, but were found to greatly dominate the maximum roll moments produced by controlled deflection of the jet vanes, which are placed very close to the center of exhaust.

Further improvements can be made to these formulations by implementing CFD with a rotating fluid domain to achieve more accurate results and verify the theoretical methods. Additionally, a method of strips along the entire rocket, rather than just the fins, coupled with Barrowman's equations for normal force coefficients of all components can be used to approximate pitch rate effects [18].

V. Conclusion

A comprehensive, medium-fidelity aerodynamic model to predict lift, drag, and moments acting on a rocket was developed in order to effectively implement active controls. Using CFD to characterize static stability and theoretical formulations to determine dynamic stability coefficients, this approach balances accuracy with computational efficiency. After its completion, the aerodynamic model was used by the GNC controls team to successfully develop trajectory simulations and implement controls. Furthermore, this approach can serve as a basis for other collegiate rocketry teams to develop and refine their own aerodynamic models. Looking ahead, future work on this topic could consist of implementing moving fluid domains to capture dynamic stability effects, robust theoretical modeling of phenomena such as body lift or Magnus effect, and transient simulations to better characterize damping and unsteady aerodynamic effects.

Acknowledgments

This work was supported by the Georgia Tech Guggenheim School of Aerospace Engineering. Special thanks is given to Ansys, Inc. for providing the software used in this study.

References

- [1] Vallini, L., "Static and Dynamic Analysis of the Aerodynamic Stability and Trajectory Simulation of a Student Sounding Rocket," Tech. rep., University of Pisa, 2014.
- [2] Niskanen, S., "OpenRocket Technical Documentation," , 2011.
- [3] Rogers, C. E., and Cooper, D., *Rogers Aeroscience RASAero II Aerodynamic Analysis and Flight Simulation Program User's Manual*, 2019.
- [4] Ou, G.-H., Li, Z.-R., Ji, W.-T., and Tao, W.-Q., "A fully coupled Pressure-Based method for compressible flows at all Mach numbers," *Applied Thermal Engineering*, Vol. 255, 2024, p. 123916. <https://doi.org/https://doi.org/10.1016/j.applthermaleng.2024.123916>, URL <https://www.sciencedirect.com/science/article/pii/S1359431124015849>.
- [5] ANSYS, "ANSYS FLUENT 12.0 Theory Guide," *ANSYS FLUENT 12.0/12.1 Documentation*, 2024.
- [6] Hinze, J., *Turbulence*, McGraw-Hill, 1975.
- [7] Greenshields, C., and Weller, H., "Notes on Computational Fluid Dynamics: General Principles," , 2022.
- [8] Apsley, D., and Leschziner, M., "Advanced turbulence modelling of separated flow in a diffuser," *Flow, turbulence and combustion*, Vol. 63, 2000, pp. 81–112. <https://doi.org/https://doi.org/10.1023/A:1009930107544>.
- [9] Menter, F. R., "Two-Equation Eddy-Viscosity Turbulence Models for Engineering Applications," *AIAA Journal*, Vol. 32, No. 8, 1994, pp. 1598–1605. <https://doi.org/10.2514/3.12149>.
- [10] Spalart, P., and Allmaras, S., "A One-Equation Turbulence Model for Aerodynamic Flows," *AIAA Journal*, Vol. 30, No. 5, 1992, pp. 876–884. <https://doi.org/10.2514/6.1992-439>.
- [11] Tong, O., *Verification and validation of the Spalart-Allmaras turbulence model for strand grids*, Utah State University, 2013.
- [12] ANSYS, "ANSYS FLUENT 12.0 User's Guide," *ANSYS FLUENT 12.0/12.1 Documentation*, 2024.
- [13] Anderson, J. D., *Fundamentals of Aerodynamics*, 6th ed., McGraw-Hill Education, 2017.
- [14] Karman, T. V., "Compressibility Effects in Aerodynamics," *Journal of the Aeronautical Sciences*, Vol. 8, No. 9, 1941. <https://doi.org/10.2514/8.10737>.
- [15] Laitone, E. V., "New Compressibility Correction for Two-Dimensional Subsonic Flow," *Journal of the Aeronautical Sciences*, Vol. 18, No. 5, 1951, pp. 350–350. <https://doi.org/10.2514/8.1951>.
- [16] Etkin, B., and Reid, L. D., *Dynamics of Flight: Stability and Control*, 3rd ed., John Wiley & Sons, 1996.
- [17] Diederich, F. W., "A plan-form parameter for correlating certain aerodynamic characteristics of swept wings," Tech. Rep. NACA-TN-2335, National Advisory Committee for Aeronautics, 1951.
- [18] Barrowman, J. S., and Barrowman, J. A., "The Theoretical Prediction of the Center of Pressure," Tech. rep., National Association of Rocketry, 1966.